ARTICLE

Open Access

Far-infrared transparent conductors

Chaoquan Hu[1]✉, Zijian Zhou[1], Xiaoyu Zhang[1], Kaiyu Guo[1], Can Cui[1], Yuankai Li[1], Zhiqing Gu[2], Wei Zhang[1,3], Liang Shen[4]✉ and Jiaqi Zhu[5]✉

Abstract
The long-standing challenge in designing far-infrared transparent conductors (FIRTC) is the combination of high plasma absorption edge (λ_p) and high conductivity (σ). These competing requirements are commonly met by tuning carrier concentration or/and effective carrier mass in a metal oxide/oxonate with low optical dielectric constant ($\varepsilon_{opt} = 2$–7). However, despite the high σ, the transparent band is limited to mid-infrared ($\lambda_p < 5$ μm). In this paper, we break the trade-off between high σ and λ_p by increasing the "so-called constant" ε_{opt} that has been neglected, and successfully develop the material family of FIRTC with $\varepsilon_{opt} > 15$ and $\lambda_p > 15$ μm. These FIRTC crystals are mainly octahedrally-coordinated heavy-metal chalcogenides and their solid solutions with shallow-level defects. Their high ε_{opt} relies on the formation of electron-deficiency multicenter bonds resulting in the great electron-polarization effect. The new FIRTC enables us to develop the first "continuous film" type far-infrared electromagnetic shielder that is unattainable using traditional materials. Therefore, this study may inaugurate a new era in far-infrared optoelectronics.

Introduction

Transparent conductor (TC) refers to materials with high transmittance and high conductivity in the interesting band[1–3]. They are widely used as key materials in optoelectronic devices, including flat-panel displays[4], solar cells[5,6], and emerging flexible[7,8] and transparent electronics[9–12]. Although TC in the visible, near-infrared, and mid-infrared bands have been developed, TC in the far-infrared band have not been designed. This greatly limits the development of far-infrared electromagnetic shielding[13,14], infrared thermal camouflage[15], photo detection[16–19], biosensing[20] technologies, and other fields. Therefore, we focus on far-infrared transparent conductors.

Transmission is a phenomenon that incident light first refracts and then passes through a medium, which is mainly affected by three absorptions of intraband transition, interband transition, and lattice vibration. The ideal condition for far-infrared transparency is that the material has extremely low light absorption in the 8–12 μm. This requires that the interband transition wavelength of the material is less than 8 μm, lattice vibration and the plasma absorption edge (λ_p) is greater than 12 μm[21]. According to Eq. 1, the λ_p depends on the speed of light C_0 and screened plasma energy (ω_p^*). ω_p^* includes both the contribution of the ion lattice background and free electron gas to the polarization response. The value of ω_p^* depends on the optical dielectric constant ε_{opt}, the effective carrier mass m^*, the carrier concentration n, the vacuum dielectric constant ε_0, and the unit charge e[21]. According to Eq. 2, the room-temperature conductivity σ depends on m^*, n, relaxation time τ, and e. From the two Equations, λ_p is proportional to m^* and inversely proportional to n, while σ is inversely proportional to m^* and directly proportional to n. Therefore, there is a trade-off between high λ_p and high σ (Fig. 1). This has proved to be a classic problem that limits the development of physics, materials, and devices of far-infrared electronics[1].

Correspondence: Chaoquan Hu (cqhu@jlu.edu.cn) or
Liang Shen (shenliang@jlu.edu.cn) or Jiaqi Zhu (zhujq@hit.edu.cn)
[1]State Key Laboratory of Superhard Materials, Key Laboratory of Automobile Materials of Ministry of Education, School of Materials Science and Engineering, Jilin Provincial International Cooperation Key Laboratory of High-Efficiency Clean Energy Materials, Jilin University, Changchun 130012, China
[2]College of Information Science and Engineering, Jiaxing University, Jiaxing 314001, China
Full list of author information is available at the end of the article

$$\lambda_P = \frac{2\pi C_0}{\omega_p^*} = 2\pi C_0 \sqrt{\frac{m^* \varepsilon_0 \varepsilon_{opt}}{ne^2}} \propto \frac{m^* \varepsilon_{opt}}{n} \quad (1)$$
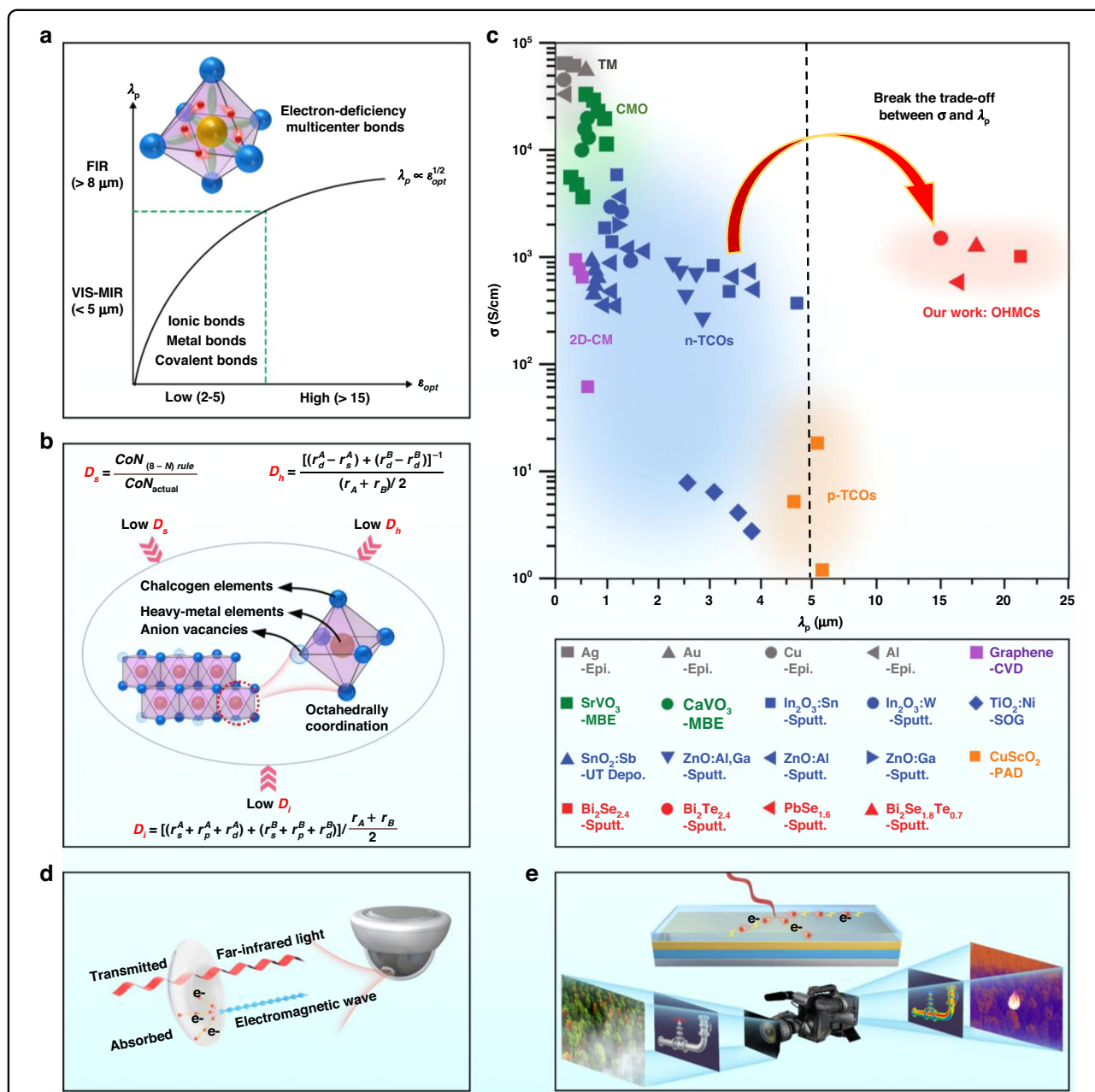
Fig. 1 Material design of far-infrared transparency and conductivity. a The positive correlation between λ_p and ε_{opt}. Typical materials with ionic, metal, and covalent bonds usually have smaller ε_{opt} and λ_p, while materials with electron-deficiency multicenter bonds have greater ε_{opt} and λ_p. **b** The three microscopic principles for the formation of the electron-deficiency multicenter bond, and the octahedrally-coordinated heavy-metal chalcogenides and their solid solutions selected by the three principles. The introduction of anion vacancies is to obtain shallow energy level defects and good conductivity. **c** The plasma absorption edge and room temperature conductivity of traditional transparent conductive materials and the four heavy-metal chalcogenides (red) that we prepared (Supplementary refs. 25–32), where gray, green, blue, orange, purple, and red represent thin metals (TM), correlated metal oxonates (CMO), n-type transparent conductive oxide (n-TCOs), p-type transparent conductive oxide (p-TCOs), 2D carbon materials (2D-CM), and octahedrally-coordinated heavy-metal chalcogenides (OHMCs), respectively. The materials and preparation methods are detailed in SI. The "continuous film" type far-infrared electromagnetic shielder (**d**) and far-infrared photodetector (**e**) based on far-infrared transparent conductors

$$\sigma = \frac{ne^2\tau}{m^*} \propto \frac{n\tau}{m^*} \tag{2}$$

Traditional transparent conductive film materials are mainly classified into the following five categories according to design strategy and chemical composition. Their σ, n, τ, m^*, ε_{opt}, and λ_p are summarized in Supplementary Information. (1) n-type transparent conductive oxide (n-TCOs)[22]. To obtain high σ, wide band gap binary oxides are used as the host, such as In_2O_3, ZnO, SnO_2, and TiO_2, and the doping concentration is maximized to ensure the electron concentration (Eq. 2). However, high electron concentration will inevitably reduce λ_p according to Eq. 1, which further decreases the infrared transmission properties (Fig. 1). (2) p-type transparent conductive oxides (p-TCOs)[23]. p-TCOs mainly includes Cu^+-based delafossites, layered oxychalcogenides, nd^6 spinel oxides, Cr^{3+}-based oxides ($3d^3$), post-transition metal oxides with lone pair state (ns^2) and some Cu^+-based halides and phosphides. The high local nature of O2p-derived valence band leads to a greater effective hole mass and low mobility. This results in that p-TCOs has a relatively large λ_p, but a low σ (Fig. 1). (3) Correlated metal oxonates[21]. In materials such as $SrVO_3$ and $CaVO_3$, m^* increases due to electron-electron interactions. It is possible to increase λ_p and maintain high n to obtain transparent conductive properties. However, λ_p is still too small because of the limited adjustment range of n and m^* of these materials (Fig. 1). (4) Thin metals (nickel, silver, copper, etc.)[24], and 2D carbon materials (graphene, carbon nanotubes)[25]. Many studies have shown that the electrical conductivity of these materials is proportional to their thickness, while the transmittance is inversely proportional to the thickness. Therefore, it is difficult to achieve a compromise between high electrical conductivity and infrared transmittance. The thin metals and 2D carbon materials generally have high electrical conductivity and poor infrared transmittance (Fig. 1). (5) Transparent conductive polymer. At present, transparent conductive polymers such as PANI:CSA and PEDOT:PSS have been used in flexible OLED devices in the visible to near-infrared band. However, these materials are not suitable for applications in the far-infrared band because of the presence of infrared absorption peaks caused by polar bonds[26]. In summary, researchers have studied the preparation, structure, and performance of various transparent conductive films and have made many important progresses. However, in these studies, researchers mainly focused on visible transparent conduction, and less attention were paid to infrared transparent conduction. Among all the materials that have been reported, the ITO film has the highest λ_p and σ compatibility. However, it can only achieve transparency within the mid-infrared band ($\lambda_p < 5\,\mu m$) under the high

conductivity ($\sigma > 1000$ S/cm). The trade-off between high λ_p and high σ are still not solved well (Fig. 1).

The ε_{opt} refers to the dielectric constant produced by electron displacement polarization in the ultraviolet-visible-near-infrared optical frequency range[27]. According to Eq. (1), a greater value of ε_{opt} can weaken the coulomb potential of ion core to free electrons, thereby increasing λ_p. However, researchers have mainly focused on the effect of n and m^* on λ_p and σ^1, ignoring the effect of the "so-called constant" ε_{opt} on increasing λ_p. The selected materials are mainly metal oxides/oxonates with small ε_{opt} (2–7). Although these materials have good electrical conductivity, the long-wave cutoff wavelength of transparent area is limited to the mid-infrared band ($\lambda_p < 5\,\mu m$). In addition, studies have reported the effect of the doping[28] and heating[29] on increasing the ε_{opt} of the dielectric material. However, the effect of structure parameters such as the coordination number on ε_{opt} has not been well explored. It is still not clear how to design high-ε_{opt} materials at the atomic level.

This paper proposes a rational design strategy that realizes the synergy of far-infrared transparency and conductivity by increasing ε_{opt} for the first time, as shown in Fig. 1. In order to design high-ε_{opt} materials, we analyze the interesting phenomenon that the ε_{opt} (29.6) of crystalline $Bi_2Se_{2.4}$ is greater than that of amorphous $Bi_2Se_{2.4}$ (9.5). This shows that the electron-deficiency multicenter bond (EDMD) formed under high coordination number are an effective way to obtain high ε_{opt} (Fig. 1a). Because EDMD increases the Bohr radius and electron delocalization, resulting in a stronger electron-polarization effect than typical ionic, metal and covalent bonds (details in SI). To predict high-ε_{opt} materials, we prove that low ionization, low hybridization, and low saturation are the three necessary principles for the formation of electron-deficiency multicenter bond (Fig. 1b). Then, we sketch the map of high-ε_{opt} materials, and discover that high-ε_{opt} materials are mainly octahedral-coordinated heavy-metal chalcogenides and their solid solutions (Fig. 1b). To obtain good electrical conductivity under the premise of far-infrared transparency, we introduce shallow energy level defects such as anion vacancies in these high-ε_{opt} crystals. This realizes the integration of far-infrared transparency and conductivity (Fig. 1c).

To verify the concept, we prepared polycrystalline octahedrally-coordinated heavy-metal chalcogenides rich in anion vacancies with a thickness of 20–160 nm: r-$Bi_2Se_{2.4}$, r-$Bi_2Te_{2.4}$, r-$Bi_2Se_{1.8}Te_{0.7}$ solid solution and c-$PbSe_{1.6}$. The results show that these materials have the characteristics of electron-deficiency multicenter bond and high ε_{opt} ($\varepsilon_{opt} > 15$). Figure 1c shows the λ_p versus σ of these four high-ε_{opt} chalcogenides and traditional transparent conducting materials. The four high-ε_{opt} chalcogenides have high σ (600–2000 S/cm) and also have much greater

λ_p (>15 µm) than that of traditional transparent conductive materials. Therefore, this new material family can be regarded as the first type of far-infrared transparent conductors (FIRTC). In addition, we develop the first "continuous film" type far-infrared electromagnetic shielder using r-Bi$_2$Se$_{2.4}$ (Fig. 1d), which have excellent performances that cannot be achieved by traditional materials. We expect that this FIRTC can also be applied to other technical fields that are beyond the reach of traditional TCs, such as far-infrared detection (Fig. 1e). This will lead to more new research into optoelectronic physics, materials, and devices.

Results

What is the microscopic origin of high ε_{opt}?

Figure 2a plots the real part of the dielectric function of amorphous and crystalline Bi$_2$Se$_{2.4}$, where the real part of the dielectric function within 2.5–3.0 µm is approximately constant. Therefore, the average value of the dielectric constant in this band is taken as ε_{opt}. This method of determining ε_{opt} has been reported in other studies[30]. The ε_{opt} of amorphous Bi$_2$Se$_{2.4}$ is 9.5. However, it is drastically increased to 29.6 after crystallization, an increase of 2 times. This indicates that the transition from amorphous to crystalline can significantly affect ε_{opt}. The dramatic

increase in ε_{opt} caused by this crystallization provides us a key to reveal the microscopic origin of high ε_{opt}.

To reveal the microscopic origin of high ε_{opt}, we used the Clausius-Mossotti equation[30] $\frac{\varepsilon_{opt}-1}{\varepsilon_{opt}+2} = \frac{N\alpha_e}{3\varepsilon_0}$ to calculate the electron polarizability α_e of the amorphous and crystalline Bi$_2$Se$_{2.4}$, as shown in Fig. 2a. As Bi$_2$Se$_{2.4}$ transformed from amorphous to crystalline, its electronic polarizability is drastically increased from 6.1 to 36.9 (details in SI). This indicates the appearance of the strong electron-polarization effect. To study the origin of the strong electronic polarization, we used the asymmetric diatomic molecular model[31] and the atomic polarizabilities of Bi and Se to calculate the polarizability of bismuth selenide under the 8-N rule (details in SI). The results show that the electronic polarizability of amorphous Bi$_2$Se$_{2.4}$ (6.1) is very close to that of bismuth selenide (7.5) under the 8-N rule. This shows that the bonding characteristics of amorphous Bi$_2$Se$_{2.4}$ conform to the 8-N rule, and its chemical bond is saturated. However, the electronic polarizability of crystalline Bi$_2$Se$_{2.4}$ (36.9) is much higher than that of bismuth selenide under the 8-N rule (7.5). This shows that another unsaturated chemical bond forms in the crystalline Bi$_2$Se$_{2.4}$.

To identify the bonding structure of crystalline Bi$_2$Se$_{2.4}$, we conducted a series of experiments and theoretical
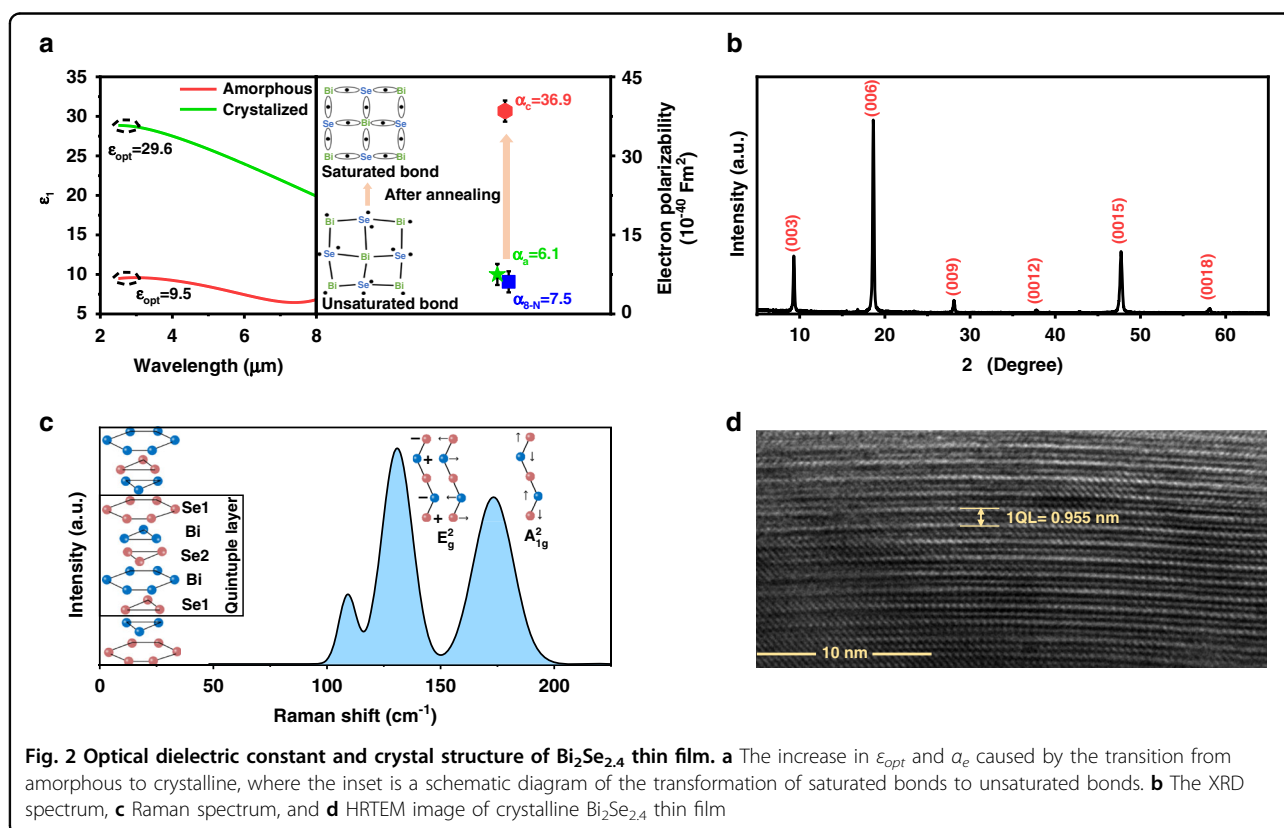
Fig. 2 Optical dielectric constant and crystal structure of Bi$_2$Se$_{2.4}$ thin film. a The increase in ε_{opt} and a_e caused by the transition from amorphous to crystalline, where the inset is a schematic diagram of the transformation of saturated bonds to unsaturated bonds. **b** The XRD spectrum, **c** Raman spectrum, and **d** HRTEM image of crystalline Bi$_2$Se$_{2.4}$ thin film

Fig. 3 Theoretical calculation and experimental characterization of r-Bi$_2$Se$_{2.4}$ bonding. a Electron density difference map of r-Bi$_8$Se$_{12}$. **b** The EELS spectrum of r-Bi$_2$Se$_{2.4}$. **c** The real (ε_1) and imaginary (ε_2) parts of r-Bi$_8$Se$_{12}$ calculated by DFT. The inset is an enlarged view of the area where ε_1 is close to zero. This indicates that there is plasma oscillation when ε_1 passes through the zero point with a positive slope. Electronic localization function of r-Bi$_8$Se$_{12}$: **d** the Se1-Bi long bond, **e** Se1-Bi short bond, **f** Bi-Se2 long bond, and **g** Bi-Se2 short bond

calculations. In an X-ray diffraction spectrum (Fig. 2b), the appearance of (003), (006), (009), (0012), (0015), and (0018) diffraction peaks indicates that Bi$_2$Se$_{2.4}$ has a rhombohedral structure and good c-axis orientation. In a Raman spectrum (Fig. 2c), the appearance of strong peaks of E^2_g and A^1_{2g} indicates that Bi$_2$Se$_{2.4}$ has a good layered structure[32]. In a HRTEM image (Fig. 2d), the film exhibits layered growth and the thickness of each QL layer is 0.955 nm. Therefore, the results indicate that the prepared Bi$_2$Se$_{2.4}$ thin film is a polycrystalline rhombohedral phase, abbreviated as r-Bi$_2$Se$_{2.4}$.

In order to further characterize the bonding structure, we established an r-Bi$_8$Se$_{12}$ unit cell and performed theoretical calculations. As shown in Fig. 3a, the electron density difference map can be divided into two parts: the surface and the body. The first and third layers of Se atoms have π electrons side by side, indicating the formation of surface π bonds[33]. In a QL layer, each Bi and six Se form six bonds, in which the bond length of four long bonds are 3.05 Å, and the bond length of two short bonds are 2.86 Å, forming an octahedron. The electron-rich

regions around the long and short bonds gradually disappear from the first layer of Se atoms (Se1) to the first layer of Bi atoms (Bi), and then to the second layer of Se atoms (Se2). This indicates that a bond of electron delocalization forms. The similar results also appear in the Electron Localization Function (ELF) spectrum. From Se1 to Bi1, and then to Se2, the ELF value of the short bond is changed from 0.64 to 0.02 (Fig. 3e, g), and the ELF value of the long bond is changed from 0.39 to 0.05 (Fig. 3d, f). These results indicate that the valence electrons in the r-Bi$_8$Se$_{12}$ unit cell are neither delocalized like the π-bond on the surface nor localized like the conventional covalent bond, but in a semi-delocalized state. This is the typical characteristic of electron-deficiency multicenter bonds (EDMB)[34]. The EDMB refers to the chemical bond formed by the superposition of the atomic orbitals of three or more atoms in a material system with a number of valence electrons less than the coordination number[35]. Low ionization, low hybridization, and low saturation are the three necessary principles for the formation of electron-deficiency multicenter bond. When Bi forms an

octahedral configuration with the surrounding 6 Se atoms, the valence electron number (5) of Bi is smaller than the coordination number (6). Accordingly, the valence electrons of Bi are not owned by a single bond, but are simultaneously shared by six surrounding Bi-Se bonds. This leads to the formation of semi-delocalized EDMB instead of localized covalent bonds between Bi and neighboring Se. Indeed, the researchers also discovered the electron-deficiency multicenter bond in heavy-metal chalcogenides such as c-PbTe[36], r-Bi$_2$Te$_3$[36], r-Sb$_2$Te$_3$[37], and c-Ge$_2$Sb$_2$Te$_5$[38] through density functional theory. They believe that this bond has a longer bond length and a higher degree of electron delocalization than conventional covalent bonds. These results are in good agreement with our calculations.

We used low energy electron loss spectroscopy (EELS) to further characterize the bonds in r-Bi$_2$Se$_{2.4}$. As shown in the EELS of r-Bi$_2$Se$_{2.4}$ (Fig. 3b), there are three characteristic peaks located at 26–28 eV, 17 eV, and 7 eV. The characteristic peaks of electron loss at 26–28 eV are consistent with the Bi5d^5 and Bi5d^3 peaks of the XPS of Bi element (details in SI). Therefore, these peaks can be attributed to Bi5d^5 and Bi5d^3 interband transitions. In the valence band spectrum of the Bi$_2$Se$_{2.4}$ film (details in SI), there are no peaks at both around 7 eV and 17 eV. However, in the real part spectrum of the dielectric function (Fig. 3c), the position of $\varepsilon_1 = 0$ corresponding to the plasma energy appeared at around 7 eV and 17 eV. These indicate that the two peaks of around 7 eV and 17 eV were not caused by interband transitions, but by two plasma oscillations. Based on the previous studies, the plasma oscillation of around 7 eV originates from surface π delocalized electrons[39], and the plasma oscillation of around 17 eV originates from the in-body electrons between delocalized and localized states[40]. Therefore, two peaks of 7 eV and 17 eV can be attributed to the surface π bond and the multicenter bond formed in r-Bi$_2$Se$_{2.4}$, respectively, which is consistent with the calculated results above. In addition, we calculated the Bohr radius of the amorphous and crystalline r-Bi$_2$Se$_{2.4}$ film through the formula in Supplementary information C3 to characterize the distance between the positive charge and the bound electron. The Bohr radius of amorphous Bi$_2$Se$_{2.4}$ is only 127 pm. However, the Bohr radius of r-Bi$_2$Se$_{2.4}$ is rapidly increased to 210 pm. This is in good agreement with the theoretical calculations and EELS results. This proves that the high ε_{opt} of r-Bi$_2$Se$_{2.4}$ originates from the formation of electron-deficiency multicenter bond, which increases the Bohr radius and electron delocalization, resulting in a strong electron-polarization effect.

What are the high-ε_{opt} materials?

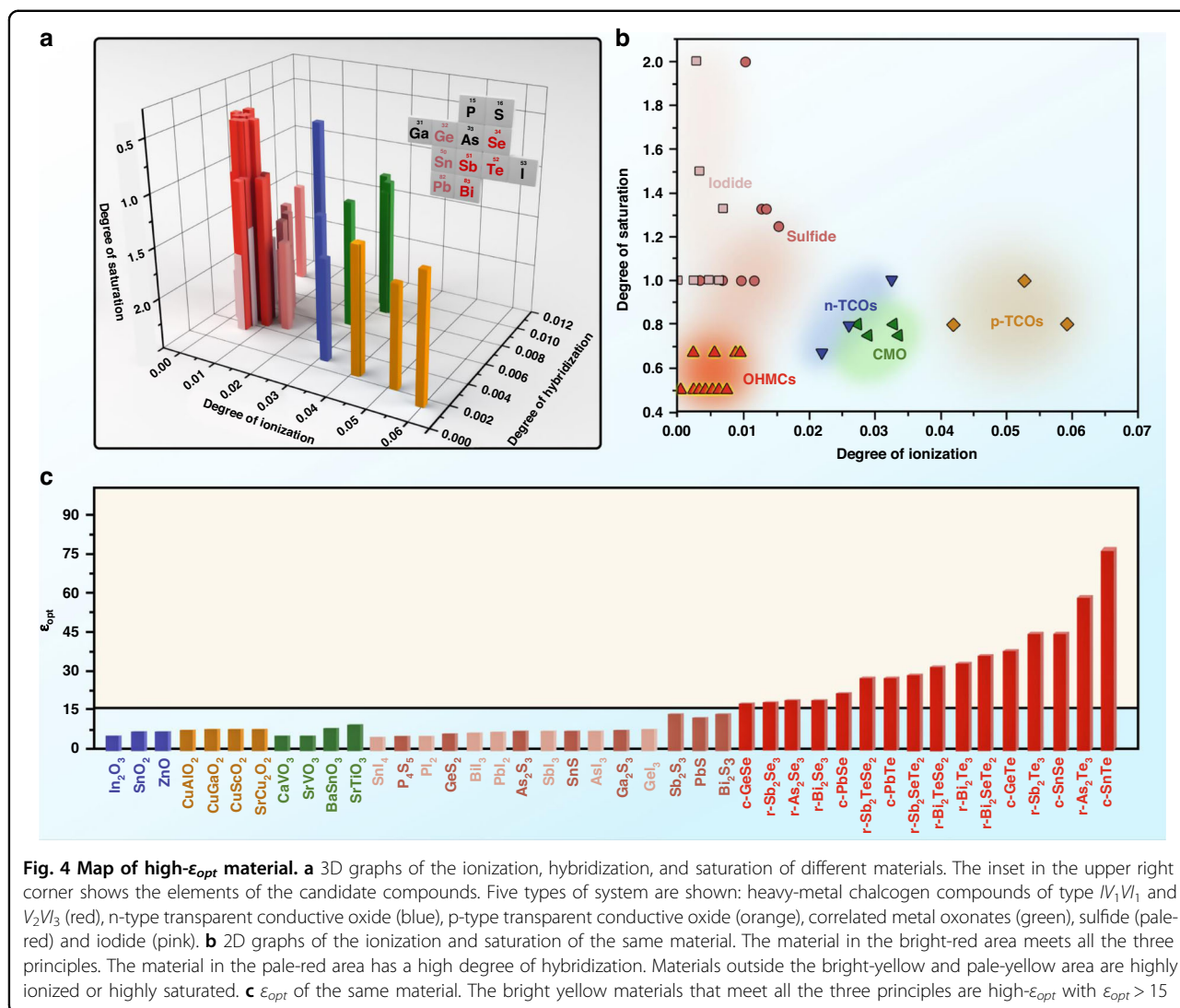In previous studies on chalcogenide phase change alloys, Wuttig et al. reported the important role of low ionization and low hybridization in the formation of semi-delocalized resonance bonds[41]. Our results of Bi$_2$Se$_{2.4}$ show that the low saturation caused by the increase of the coordination number also plays an important role in the generation of electron-deficiency multicenter bonds. Therefore, we proposed the following three microscopic principles for designing high-ε_{opt} crystals with electron-deficiency multicenter bonds (details in SI). (1) Low degree of ionization (D_i). D_i is the difference between the sum of the s-, p-, d-orbital radii of cations M and anions N[41] (Eq. 3). The greater the D_i, the more likely M and N atoms are to form ionic bonds by gaining or losing electrons. (2) Low degree of hybridization (D_h). The D_h is defined as the reciprocal of the sum of the difference between the outermost d-orbital and innermost s-orbital radii of cations M and anions N[41] (Eq. 4). The greater the D_h, the more likely the M and N atoms to form a covalent bond by sharing valence electrons. (3) Low degree of saturation (D_s). The D_s is the ratio of the coordination number of atoms under the 8-N rule to the actual coordination number[37] (Eq. 3). *No.* refers to the number of valence electrons of the atom. The actual coordination number is the number of nearest neighbors of the reference atom in the actual crystal structure.

$$D_i = \left[\left(r_s^M + r_p^M + r_d^M \right) + \left(r_s^N + r_p^N + r_d^N \right) \right] / \frac{r_M + r_N}{2} \quad (3)$$

$$D_h = \left[\left(r_d^M - r_s^M \right) + \left(r_d^N - r_s^N \right) \right]^{-1} / \frac{r_M + r_N}{2} \quad (4)$$

$$D_s = \frac{CoN_{(8-No.)rule}}{CoN_{actual}} \quad (5)$$

To predict more high-ε_{opt} candidate materials, we used the above three microscopic principles to establish a three-dimensional coordinate system (Fig. 4a), and predicted the possible compounds in the figure. We selected the cations M and anions N in the compound based on the following criteria. (1) To obtain a low degree of ionization, degree of hybridization, and a high coordination number equal to or greater than 6, the electronegativity of anions N should be small, the number of periods should be large, and the number of valence electrons should be large. Therefore, the heavy atoms S, Se, and Te of the *VIA* group were mainly selected as anions N (Fig. 4a). The heavier I atom was also selected for the comparison. (2) To obtain low degree of ionization, degree of hybridization, and unsaturated bond, the electronegativity and period number of cations M should be as large as possible, and the number of valence electrons should be less than 6. Therefore, the heavy atoms Sn, Pb, Sb, and Bi of the *IVA* and *VA* groups were mainly selected as the cations M

Fig. 4 Map of high-ε_{opt} material. a 3D graphs of the ionization, hybridization, and saturation of different materials. The inset in the upper right corner shows the elements of the candidate compounds. Five types of system are shown: heavy-metal chalcogen compounds of type IV_1VI_1 and V_2VI_3 (red), n-type transparent conductive oxide (blue), p-type transparent conductive oxide (orange), correlated metal oxonates (green), sulfide (pale-red) and iodide (pink). **b** 2D graphs of the ionization and saturation of the same material. The material in the bright-red area meets all the three principles. The material in the pale-red area has a high degree of hybridization. Materials outside the bright-yellow and pale-yellow area are highly ionized or highly saturated. **c** ε_{opt} of the same material. The bright yellow materials that meet all the three principles are high-ε_{opt} with $\varepsilon_{opt} > 15$

(Fig. 4a). (3) To predict more high-ε_{opt} candidate materials, the atomic composition, stoichiometric ratio, and crystal structure of the materials in this paper were diverse. These materials could be prepared and were all reported in existing literatures.

In Fig. 4a, the degree of ionization, degree of hybridization, and degree of saturation of r-Bi_2Se_3 are only 7.5 E + 03, 4.7 E − 03, and 0.5. Therefore, the electrons will not locally form an ionic bond around an atom, nor will it locally form a covalent bond between two atoms. They are shared by multiple atoms, forming highly delocalized electron-deficiency multicenter bonds. Since the increase in the degree of ionization, degree of hybridization, or degree of saturation will increase the localization of valence electrons near the ionic substance, typical multi-center bond materials should be mainly formed in a small area near r-Bi_2Se_3. A side view of Fig. 4a was provided in Fig. 4b to show it more clearly. The bright-red area is the

low degree of ionization, low degree of hybridization and low degree of saturation area. That is, it meets all the three principles. The material in the pale-red area has a high degree of hybridization. Materials outside the red area are highly ionized or highly saturated. Figure 4c shows the ε_{opt} of all the materials in Fig. 4b (details in SI). The results are in agreement with our prediction. The materials that meet all the three principles are high-ε_{opt} materials, and materials that do not meet any of the principles are low-ε_{opt} materials. Among these low-ε_{opt} materials, some materials (In_2O_3:Sn) have a high degree of ionization, and some materials ($SrVO_3$) have a high degree of hybridization. Iodine and chalcogen compounds, such as BiI_3 and Bi_2S_3, have the low degree of ionization and degree of hybridization. However, since their degrees of saturation are too great, they do not have a high ε_{opt}. These results prove that low degree of ionization, low degree of hybridization and low degree of
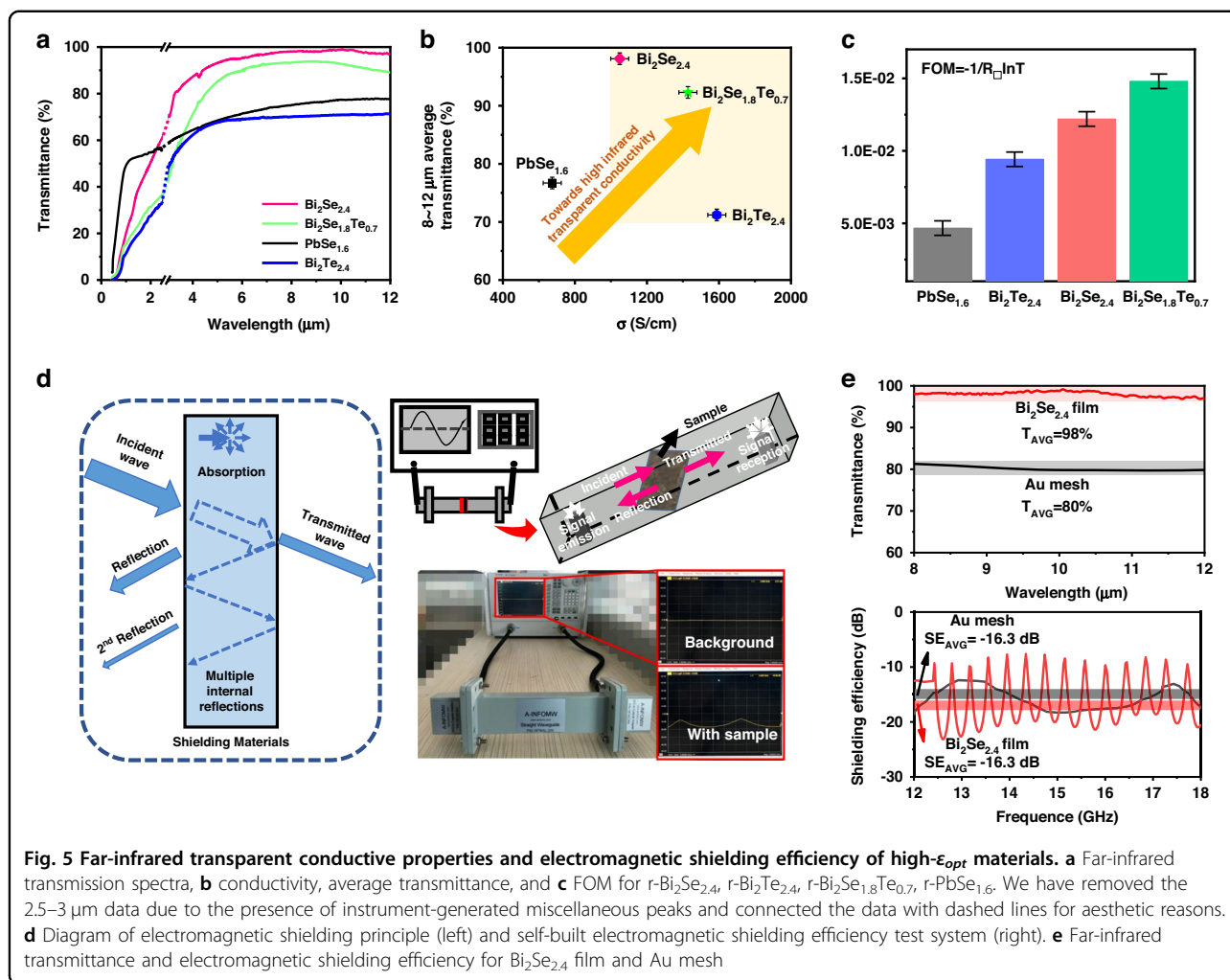
Fig. 5 Far-infrared transparent conductive properties and electromagnetic shielding efficiency of high-ε_{opt} materials. a Far-infrared transmission spectra, **b** conductivity, average transmittance, and **c** FOM for r-$Bi_2Se_{2.4}$, r-$Bi_2Te_{2.4}$, r-$Bi_2Se_{1.8}Te_{0.7}$, r-$PbSe_{1.6}$. We have removed the 2.5–3 μm data due to the presence of instrument-generated miscellaneous peaks and connected the data with dashed lines for aesthetic reasons. **d** Diagram of electromagnetic shielding principle (left) and self-built electromagnetic shielding efficiency test system (right). **e** Far-infrared transmittance and electromagnetic shielding efficiency for $Bi_2Se_{2.4}$ film and Au mesh

saturation are the three necessary principles for the formation of high-ε_{opt} crystals.

In Fig. 4, high-ε_{opt} materials are mainly heavy-metal chalcogenides in octahedral configuration including r-Bi_2Se_3, r-Sb_2Te_2Se, r-As_2Te_3, r-Bi_2STe_2, r-Bi_2Te_3, r-Sb_2Te_3, c-SnTe, c-PbSe, c-PbTe. Their phase characteristics and chemical formula can be described as: (1) r-M_2N_3 with rhombohedral structure (M = Bi, Sb, As, etc., N = Se, Te, Se+Te); (2) c-M_1N_1 with cubic structure (M = Pb, Sn, etc., N = Se, Te, Se+Te).

Can high ε_{opt} really break the far-infrared transparent and conductive trade-off?

To verify that the high-ε_{opt} material is a potential FIRTC, we tested the infrared transmittance and conductivity at room temperature of r-$Bi_2Se_{2.4}$ with Se vacancies and different film thicknesses (details in SI). The results are shown in Fig. 5a, Fig. S7, and Fig. 5b. The conductivity of r-$Bi_2Se_{2.4}$ film is 1049.4 S/cm. The transmittances of 3–5 μm and 8–12 μm in the two atmospheric

windows are as high as 85% and 98%, respectively. These indicators have exceeded the application requirements of infrared transparent conductive film (conductivity is 1000 S/cm, transmittance is 70%). This shows that r-$Bi_2Se_{2.4}$ film is a wide-band infrared TC. In Figure S7, the λ_p of traditional transparent conductive materials, such as n-type oxides (ITO), p-type oxides ($CuScO_2$), ultra-thin metals (Ag), and correlated metal oxonates ($SrVO_3$), are all less than 5 μm. The far-infrared transparent conductive properties of r-$Bi_2Se_{2.4}$ film are not possessed by other traditional materials. Therefore, it can be regarded as the first FIRTC.

We first explain the reasons for the high conductivity of r-$Bi_2Se_{2.4}$ film. We find that the Hall coefficient of the r-$Bi_2Se_{2.4}$ film is negative ($R_H = -0.05$) through the Hall effect test (details in SI). This indicates that the conduction mode of the film is electronic conduction. The electrons in the film mainly come from Se vacancies. Se vacancies, as a kind of shallow energy level defect, can generate free electrons through thermal excitation at

room temperature[42]. Studies revealed that Se vacancies in bismuth selenide films are mainly derived from the evaporation of Se atoms during film sputtering[43]. Because among all types of point defects (vacancies, interstitial atoms, and anti-site atoms) Se vacancies have the lowest formation energy and are most easily formed in selenium-deficient bismuth selenide[44]. In Table S1, the electron concentration of $Bi_2Se_{2.4}$ film is much smaller than that of ITO, and its relaxation time is much larger than that of ITO. Also, both materials have similar effective masses[43,45]. Therefore, $Bi_2Se_{2.4}$ has a high conductivity because of its high relaxation time. The high relaxation time of $Bi_2Se_{2.4}$ mainly comes from two aspects. One is that r-Bi_2Se_3 crystal has higher intrinsic mobility, which can be attributed to its smaller effective mass and larger deformation potential energy[46]. The second is that the electron concentration of r-$Bi_2Se_{2.4}$ film is lower. This reduces the collision between electrons. The detailed discussion is provided in Supplementary information B8.

Next, we discuss the reasons for the excellent far-infrared transmission of r-$Bi_2Se_{2.4}$ film. The frequency corresponding to $\varepsilon_r = 0$ in the dielectric real part spectrum is taken as the plasma frequency ω_p to obtain λ_p (details in SI). In Fig. S7, the λ_p of r-$Bi_2Se_{2.4}$ film (21.4 μm) is much larger than that of ITO (1.5 μm), which is mainly due to the great shielding effect from high ε_{opt} of r-$Bi_2Se_{2.4}$. This weakens the coulomb effect of the ion on the free electrons, which in turn increases the λ_p (Eq. 1). λ_p of r-$Bi_2Se_{2.4}$ is 21.4 μm, which is far greater than 12 μm. Hence, its interband transition absorption hardly occurs in the far-infrared band (8–12 μm) we focus on in this article. In addition, it is shown that the band gap (E_g) and transverse optical branch vibration frequency (ω_{TO}) of the r-$Bi_2Se_{2.4}$ film are 0.55 eV (details in SI) and 0.03 eV[47], respectively. This makes the interband transition absorption and lattice vibration absorption of the r-$Bi_2Se_{2.4}$ film in the band less than 2.5 μm and in the band centered at 41 μm, respectively, far away from the far-infrared band. These are the reasons for excellent far-infrared transmission of the r-$Bi_2Se_{2.4}$ film.

To further optimize the phase structure and atomic composition for better far-infrared transparent conductive properties, we prepared other typical candidate materials under similar experimental condition as r-$Bi_2Se_{2.4}$, including r-$Bi_2Te_{2.4}$, r-$Bi_2Se_{1.8}Te_{0.7}$, and c-$PbSe_{1.6}$. Their composition, structure, and transparent conductive properties under different thicknesses are shown in Supplementary information. Their transmittance and electrical conductivity are shown in Fig. 5a, b. From Fig. 5a, the transmittance of all four film samples in 8–12 μm is all over 60%, with that of r-$Bi_2Se_{2.4}$ and r-$Bi_2Se_{1.8}Te_{0.7}$ exceeding 90%, which is attributable to the large λ_p, and the lack of lattice vibration absorption and interband transition absorption. In 3–8 μm, these four samples still have high transmittance. In 0.4–2.5 μm, however, the transmittance decreases to 0 below the interband transition absorption wavelength. All materials have far-infrared transparent and conductive properties, indicating that increasing the ε_{opt} is an effective and universal strategy to break the trade-off between far-infrared transparency and conductivity. The Hall coefficients of all these films are negative through the Hall test. This indicates that their main carriers are free electrons. We used a figure of merit (FOM) to quantitatively describe the transparent conduction properties of the material (details in SI), and the results are shown in Fig. 3c. Both average transmittance and conductivity of c-$PbSe_{1.6}$ are lower than that of other rhombohedral films. This indicates that the rhombohedral phase is more favorite to high transparent conductive properties. This is because the rhombohedral phase is mainly composed of group VA elements and VIA elements, and the cubic phase is mainly composed of group IVA elements and VIA elements. The bond saturation of the former (0.50) is lower than that of the latter (0.67), which favors the high ε_{opt}. In all rhombohedral films, the FOM of r-$Bi_2Se_{1.8}Te_{0.7}$ is significantly greater than that of both r-$Bi_2Se_{2.4}$ and r-$Bi_2Te_{2.4}$. This is because r-$Bi_2Se_{1.8}Te_{0.7}$ has not only a high ε_{opt} (27.0), but also a moderate carrier concentration (1.2 E + 20 cm^{-3}). Therefore, among all the high-ε_{opt} chalcogenides, the heavy-metal selenium telluride in octahedral configuration has the best comprehensive properties.

An important application of FIRTC is the electromagnetic shielders for far-infrared windows. Since there was no far-infrared transparent conductive material in the past, the traditional electromagnetic shielder for the far-infrared window is mainly a metal mesh such as Au. In this paper, to explore the application potential of the r-$Bi_2Se_{2.4}$ film, we used our own assembled test device (Fig. 5d) to estimate the electromagnetic shielding efficiency. In Fig. 5d, the left diagram describes the interaction of electromagnetic waves and shielding materials. When electromagnetic waves are incident on the surface of the shielding material, a portion of the electromagnetic waves are reflected on the outer surface. Then, the remaining electromagnetic waves enter the material and are reflected multiple times between the two interfaces. In this process, the energy of light is continuously attenuated. Eventually, the unabsorbed electromagnetic waves pass through the shielding material. The right diagram describes the working principle and actual image of the electromagnetic shielding test system. The results are shown in Fig. 5e. The performance of the traditional Au mesh is provided for the comparison. As shown in Fig. 5e, the electromagnetic shielding efficiency of the r-$Bi_2Se_{2.4}$ film is SE = −16.3 dB, which is very close to that of the Au mesh (SE = −15.7 dB). The average transmittance of the r-$Bi_2Se_{2.4}$ film in the 3−5

and 8–12 µm bands is 86 and 98%, respectively, which are greater than that of the Au mesh (T = 87%, 80%)[48]. Therefore, the new far-infrared transparent conductive film in this paper has good application prospects, and the bottleneck problems of poor imaging quality and complex processing of traditional far-infrared electromagnetic shielding mesh is expected to be solved.

Based on good electrical conductivity and infrared transmission, our FIRTC may also be applied to photodetectors and invisible sensors. As an important part of the optical fiber communication system, the photodetector is a component that converts optical signals into electrical signals. It is widely applied in optical communication[12], laser guidance[19], biosensing[20], etc. If the transparent electrode is replaced from the traditional ITO to our FIRTC, the applicable band of the photodetector can be complemented to far-infrared region, which will promote the development of far-infrared search and guidance technology. The invisible sensor[15] is a new type of sensor that can effectively hide its own thermal and electronic signals and it can be applied to infrared thermal camouflage, infrared photoelectric countermeasures, and other fields. If our FIRTC is applied to the camouflage shell, the invisible sensor is expected to disguise the target under multiple physical fields such as infrared light, electricity, and heat, which will facilitate the development of technologies such as infrared camouflage and infrared remote sensing.

Discussion

In conclusion, we prove that increasing the optical dielectric constant is an effective and universal strategy to break the trade-off between infrared transparency and conductivity through experiments and theoretical calculations. We have obtained the first family of far-infrared TCs. Using this type of materials, we have developed the first "continuous film" type far-infrared electromagnetic shielder. Unlike the well-known transparent conductive material ITO (indium-tin oxide), which is used in the visible band, the material we have developed is a transparent conductive material used in the far-infrared band, called "FIRTC". We expect that this "FIRTC" can be applied to the technical fields that are beyond the reach of traditional visible ITO, such as photodetectors, invisible sensors, etc. This will lead to more new research into optoelectronic physics, materials, and devices.

Materials and methods
Material preparation

Using magnetron sputtering, we simultaneously deposited thin films on single-crystal Si, polycrystalline zinc sulfide and glass at the same time. Among them, single-crystal Si is used for structural testing of thin film samples, polycrystalline zinc sulfide for infrared transmission spectrum and electrical tests, and glass for visible light transmission spectrum tests. Before thin film deposition, the substrate was sequentially placed in acetone, alcohol, and deionized water for ultrasonic vibration cleaning, and then they were introduced into the sputtering vacuum chamber (base pressure $4*10^{-4}$ Pa). To obtain Bi_2Se_x, Bi_2Te_x, $Bi_2Se_xTe_y$, $PbSe_x$, and In_2O_3:Sn films, the high-purity Bi_2Se_3 (99.99%), Bi_2Te_3 (99.99%), PbSe (99.99%), and $In_{1.7}Sn_{0.3}O_3$ (99.99%) targets are sputtered in a pure Ar atmosphere. The $Bi_2Se_xTe_y$ was obtained by co-sputtering Bi_2Se_3 and Bi_2Te_3 targets. During the sputtering process, the deposition parameters were set as follows: substrate temperature: 200–300 °C; substrate bias: floating; RF power applied to the targets: 60–90 W; pressure: 1 Pa; deposition time: 15–300 s. In addition, a tube furnace was used to anneal the obtained film at a high temperature in an Ar atmosphere. To prevent the Se in the film from evaporating, we placed a small amount of Se particles in the tube furnace to create a Se atmosphere. The heating rate was 5 °C/min, the annealing temperature was 200–400 °C, and the holding time was 10–30 min. The detailed preparation and annealing conditions, and the thickness of each film are listed in Supplementary information G1.

Material characterization

Surface profiler (Bruker, Inc., DEKTAK PROFILER 150) was used to characterize the thickness of the films. X-ray photoelectron spectroscopy (VG Scientific Ltd, Inc., VG ESCALAB MK II) and energy dispersive spectrometer equipped in a field-emission scanning electron microscope (SU8010, Hitachi, Tokyo, Japan) were used to measure the composition of the films. Atomic force microscope (Bruker, Inc., Dimension Icon) was used to characterize the surface morphology of the films. The high-resolution transmission electron microscopy (JEM-2100F, JEOL, Tokyo, Japan), grazing-incidence X-ray diffraction (Bruker, Inc., D8-tools XRD), Raman (B&W TEK, Inc., GlacierTM T), Electron Energy-loss spectroscopy (EELS) (JEOL, Inc., JEM-ARM300F) and XPS valence band spectra were used to characterize the structure and chemical bonding of the films. Ultraviolet-visible-near infrared photometer (Perkin Elmer, Inc., Lambda 950) and Fourier transform infrared spectroscopy (Perkin Elmer, Inc., Spectrum One) were used to test the transmittance of the film at 200–2500 nm and 2500–16000 nm. The electrical properties of the film such as conductivity, sheet resistance, carrier concentration, and mobility were measured by Hall tester (CH Electronic Devices, Inc., CH-50), detailed in supporting information.

First-principles calculations

Our first-principles calculations for the electronic structure of Bi_2Se_3 with rhombohedral phase (space group R-3m) were performed using the VASP module, on the

basis of the density functional theory (DFT) combined with the projector augmented wave (PAW) method. The exchange correlation effect was described by generalized gradient approximation (GGA) in Perdew–Burke–Ernzerhof (PBE) functional form. The structure was fully relaxed until the total energy converges to below than 10^{-4} eV, in which a kinetic energy cut-off for the plane wave of 550 eV was used to minimize the local energy. The optimized Bi_2Se_3 geometrical structure with a lattice parameter of 10.42 Å, which is consistent with the experimental value (10.40 Å)[33,49].

Spectrum fitting

To obtain the dielectric function spectrum of the film, we used the Drude-Lorentz model to fit the infrared transmission spectrum. The formulas are

$$\varepsilon(E) = \varepsilon_\infty - \frac{E_p^2}{E^2 - i\Gamma_D E} + \sum_{j=1}^{n} \frac{S_j E_{0j}^2}{E_{0j}^2 - E^2 + iE\Gamma_i}, \ n = 1, 2, 3 \quad (6)$$

$$n(E) = \frac{1}{\sqrt{2}} \left[\sqrt{\varepsilon_1^2(E) + \varepsilon_2^2(E)} + \varepsilon_1(E) \right]^{1/2} \quad (7)$$

$$k(E) = \frac{1}{\sqrt{2}} \left[\sqrt{\varepsilon_1^2(E) + \varepsilon_2^2(E)} - \varepsilon_1(E) \right]^{1/2} \quad (8)$$

where ε_1 and ε_2 are the real and imaginary parts of the dielectric function. S, E_0, and Γ are the amplitude, the energy of the transition center, and the broadening term, respectively. ε_∞ is the high-frequency dielectric constant, and E is the incident photon energy. E_p is the plasma energy, and proportional to the free electron concentration of the material. Γ_D is the relaxation energy. The transmittance of the substrate film can be obtained from Eqs. (9) and (10):

$$\begin{bmatrix} B \\ C \end{bmatrix} = \begin{bmatrix} \cos\delta_1 & \frac{i}{\eta_1}\sin\delta_1 \\ i\eta_1\sin\delta_1 & \cos\delta_1 \end{bmatrix} \begin{bmatrix} 1 \\ \eta_2 \end{bmatrix} \quad (9)$$

where the phase difference is $\delta_1 = \frac{2\pi}{\lambda}(n + ik)d$, the film thickness is d, the admittance of the film $\eta_1 = N = n - ik$, and the admittance of the substrate is η_2.

$$T = \frac{4n_0\eta_2}{(B + C)(B + C)} \quad (10)$$

Substituting the expressions of $\varepsilon_1(E)$ and $\varepsilon_2(E)$ into Eqs. (7) and (8), and substituting the obtained expressions into Eqs. (9) and (10), the transmittance function used to fit the experimental data is as follows:

$$T(E) = \frac{[n(E) - 1]^2 + k^2(E)}{[n(E) + 1]^2 + k^2(E)} \quad (11)$$

The optical dielectric constant ε_{opt} of the film and the absorption edge (λ_p) are obtained through the dielectric function spectrum, detailed in the supplementary information.

Electromagnetic shielding test platform and performance evaluation

An electromagnetic shielding test system was established with a vector network analyzer (Agilent, Inc., N523xA PNA-L) as the core. We used this system to obtain the electromagnetic shielding effectiveness of the film sample in the 12–18 GHZ frequency band, more details of the device and test are shown in the supplementary information.

Author details
[1]State Key Laboratory of Superhard Materials, Key Laboratory of Automobile Materials of Ministry of Education, School of Materials Science and Engineering, Jilin Provincial International Cooperation Key Laboratory of High-Efficiency Clean Energy Materials, Jilin University, Changchun 130012, China. [2]College of Information Science and Engineering, Jiaxing University, Jiaxing 314001, China. [3]Electron Microscopy Center, Jilin University, Changchun 130012, China. [4]State Key Laboratory of Integrated Optoelectronics, College of Electronic Science and Engineering, International Center of Future Science, Jilin University, Changchun 130012, China. [5]National Key Laboratory of Science and Technology on Advanced Composites in Special Environments, Harbin Institute of Technology, Harbin 150080, China

Conflict of interest
The authors declare no competing interests.

References
1. Gao, J. et al. Physics of transparent conductors. *Adv. Phys.* **65**, 553–617 (2016).
2. Hosono, H. et al. P-type electrical conduction in transparent thin films of CuAlO$_2$. *Nature* **389**, 939–941 (1997).
3. Chen, Z. & Segev, M. Highlighting photonics: looking into the next decade. *eLight* **1**, 2 (2021).
4. Matsushima, T. et al. High performance from extraordinarily thick organic light-emitting diodes. *Nature* **572**, 502–506 (2019).
5. Han, Q. F., Hsieh, Y. T., Meng, L. & Yang, Y. High-performance perovskite/Cu(In,Ga)Se$_2$ monolithic tandem solar cells. *Science* **361**, 904–908 (2018).
6. Brinkmann, K. O. et al. Perovskite-organic tandem solar cells with indium oxide interconnect. *Nature* **604**, 280–286 (2022).
7. Chen, Z. H., Fang, R., Li, W. & Guan, J. Stretchable transparent conductors: from micro/macromechanics to applications. *Adv. Mater.* **31**, e1900756 (2019).

8. Datta, R. S. et al. Flexible two-dimensional indium tin oxide fabricated using a liquid metal printing technique. *Nat. Electron.* **3**, 51–58 (2020).

9. Yu, X., Marks, T. J. & Facchetti, A. Metal oxides for optoelectronic applications. *Nat. Mater.* **15**, 383–396 (2016).

10. Ellmer, K. Past achievements and future challenges in the development of optically transparent electrodes. *Nat. Photonics* **6**, 809–817 (2012).

11. Li, H. et al. Revealing the output power potential of bifacial monolithic all-perovskite tandem solar cells. *eLight* **2**, 21 (2022).

12. Maniyara, R. A. et al. Highly transparent and conductive ITO substrates for near infrared applications. *APL Mater.* **9**, 021121 (2021).

13. Zeng, Z. et al. Flexible and ultrathin waterproof cellular membranes based on high-conjunction metal-wrapped polymer nanofibers for flectromagnetic interference shielding. *Adv. Mater.* **32**, e1908496 (2020).

14. Wang, J. et al. Ultra-high electrical conductivity in filler-free polymeric hydrogels toward thermoelectrics and electromagnetic interference shielding. *Adv. Mater.* **34**, e2109904 (2022).

15. Yang, T. et al. Invisible sensors: simultaneous sensing and camouflaging in multiphysical fields. *Adv. Mater.* **27**, 7752–7758 (2015).

16. Palaferri, D. et al. Room-temperature nine-microm-wavelength photodetectors and GHz-frequency heterodyne receivers. *Nature* **556**, 85–88 (2018).

17. Maiti, R. et al. Strain-engineered high-responsivity $MoTe_2$ photodetector for silicon photonic integrated circuits. *Nat. Photonics* **14**, 578–584 (2020).

18. Hu, C., Wang, X. & Song, B. High-performance position-sensitive detector based on the lateral photoelectrical effect of two-dimensional materials. *Light Sci. Appl.* **9**, 88 (2020).

19. Mehrabi, J. N., Kelly, K. M., Holmes, J. D. & Zachary, C. B. Assessing the outcomes of focused heating of the skin by a long-pulsed 1064 nm laser with an integrated scanner, infrared thermal guidance, and optical coherence tomography. *Lasers Surg. Med.* **53**, 806–814 (2021).

20. Zhang, L. et al. Metaoptronic multiplexed interface for probing bioentity behaviors. *Nano Lett.* **21**, 2681–2689 (2021).

21. Zhang, L. et al. Correlated metals as transparent conductors. *Nat. Mater.* **15**, 204–210 (2016).

22. Dixon, S. C., Scanlon, D. O., Carmalt, C. J. & Parkin, I. P. n-Type doped transparent conducting binary oxides: an overview. *J. Mater. Chem. C.* **4**, 6946–6961 (2016).

23. Willis, J. & Scanlon, D. O. Latest directions in p-type transparent conductor design. *J. Mater. Chem. C.* **9**, 11995–12009 (2021).

24. Yun, J. Ultrathin metal films for transparent electrodes of flexible optoelectronic devices. *Adv. Funct. Mater.* **27**, 1606641 (2017).

25. Song, Y., Fang, W., Brenes, R. & Kong, J. Challenges and opportunities for graphene as transparent conductors in optoelectronics. *Nano Today* **10**, 681–700 (2015).

26. Joo, Y., Agarkar, V., Sung, S. H., Savoie, B. M. & Boudouris, B. W. A non-conjugated radical polymer glass with high electrical conductivity. *Science* **359**, 1391–1395 (2018).

27. Cochran, W. *The Structure and Properties of Solids* (Edward Arnold, 1973).

28. Gor'kov, L. P. Phonon mechanism in the most dilute superconductor n-type $SrTiO_3$. *Proc. Natl Acad. Sci. USA* **113**, 4646–4651 (2016).

29. Larijani, M. M., Hasani, E. & Safa, S. Annealing temperature effect on the optical properties of thermally oxidized nano-crystalline ZrO_2 thin films grown on glass substrates. *Appl. Surf. Sci.* **290**, 490–494 (2014).

30. Shportko, K. et al. Resonant bonding in crystalline phase-change materials. *Nat. Mater.* **7**, 653–658 (2008).

31. Fujiwara, H. & Kondo, M. Effects of carrier concentration on the dielectric function of ZnO:Ga and In_2O_3:Sn studied by spectroscopic ellipsometry: analysis of free-carrier and band-edge absorption. *Phys. Rev. B* **71**, 075109 (2005).

32. Huang, Fei et al. Raman Spectra of Bi_2Se_3 single crystals at different laser wavelengths and powers. *J. Chin. Ceram. Soc.* **47**, 514–518 (2019).

33. Shu, G. J. et al. dynamic surface electronic reconstruction as symmetry-protected topological orders in topological insulator Bi_2Se_3. *Phys. Rev. Mater.* **2**, 044201 (2018).

34. Lee, T. H. & Elliott, S. R. Multi-center hyperbonding in phase-change materials. *Phys. Status Solidi-Rapid Res. Lett.* **15**, 2000516 (2021).

35. Pendas, A. M. & Francisco, E. Chemical bonding from the statistics of the electron distribution. *Chem. Phys. Chem.* **20**, 2722–2741 (2019).

36. Lee, S. et al. Resonant bonding leads to low lattice thermal conductivity. *Nat. Commun.* **5**, 3525 (2014).

37. Cheng, Y. et al. Understanding the structure and properties of sesqui-chalcogenides (i.e., V_2VI_3 or Pn_2Ch_3 (Pn = pnictogen, Ch = chalcogen) compounds from a bonding perspective. *Adv. Mater.* **31**, e1904316 (2019).

38. Lee, T. H. & Elliott, S. R. Chemical bonding in chalcogenides: the concept of multicenter hyperbonding. *Adv. Mater.* **32**, e2000340 (2020).

39. Nascimento, V. B. et al. XPS and EELS study of the bismuth selenide. *J. Electron Spectrosc. Relat. Phenom.* **104**, 99–107 (1999).

40. Kogar, A. et al. Surface collective modes in the topological insulators Bi_2Se_3 and $Bi_{0.5}Sb_{1.5}Te_{3-x}Se_x$. *Phys. Rev. Lett.* **115**, 257402 (2015).

41. Lencer, D. et al. A map for phase-change materials. *Nat. Mater.* **7**, 972–977 (2008).

42. Wang, S. & Zhang, P. Native point defects in Bi_2Se_3: a first-principles study. *Phys. Lett. A* **384**, 126281 (2020).

43. Heremans, J. P., Cava, R. J. & Samarth, N. Tetradymites as thermoelectrics and topological insulators. *Nat. Rev. Mater.* **2**, 17049 (2017).

44. Xue, L. et al. First-principles study of native point defects in Bi_2Se_3. *AIP Adv.* **3**, 052105 (2013).

45. Hautier, G., Miglio, A., Waroquiers, D., Rignanese, G.-M. & Gonze, X. How does chemistry influence electron effective mass in oxides? a high-throughput computational analysis. *Chem. Mat.* **26**, 5447–5458 (2014).

46. Liu, Y., Xu, Y., Ji, Y. & Zhang, H. Monolayer $Bi_2Se_{3-x}Te_x$: novel two-dimensional semiconductors with excellent stability and high electron mobility. *Phys. Chem. Chem. Phys.* **22**, 9685–9692 (2020).

47. Richer, W., Koiiler, H. & Becker, C. R. A Raman and far-infrared investigation of phonons in the Rhombohedra1 V_2-VI_3 Compounds. *Phys. Status Solidi B-Basic Res.* **84**, 619–628 (1977).

48. Cat, Y., Baran, V. & Ozcelik, S. EMI shielding effectiveness and heater behavior for Ge IR Windows. *Phys. Status Solidi A-Appl. Mat.* **216**, 065501 (2019).

49. Ptok, A., Kapcia, K. J. & Ciechan, A. Electronic properties of Bi_2Se_3 dopped by 3d transition metal (Mn, Fe, Co, or Ni) ions. *J. Phys. Condens. Matter* **33**, 065501 (2021).